Strong tectonic and weak climatic control on exhumation rates in the Venezuelan Andes

Mauricio M.A. Bermúdez, Pieter van Der Beek, Matthias Bernet

Strong tectonic and weak climatic control on exhumation rates in the Venezuelan Andes

Mauricio A. Bermúdez[a,b], Peter A. van der Beek[b], Matthias Bernet[b]

[a]Laboratorios de Termocronología y Geomatemáticas, Escuela de Geología, Minas y Geofísica. Facultad de Ingeniería, Universidad Central de Venezuela, Caracas, Venezuela. (mauricio.bermudez@ing.ucv.ve/ Fax: +58 212 6053120/ Phone: +58 212 6053123)

[b]Institut des Sciences de la Terre (ISTerre), Université Joseph Fourier, CNRS, BP 53, 38041 Grenoble cedex 9, France.

6310 Words

7 Figures, 3 Tables

83 References

16 **ABSTRACT**

17

18 We have studied the relationships between present day relief, precipitation, stream power,
19 seismic energy, seismic strain rate and long-term exhumation rates for the Venezuelan Andes.
20 Average long-term exhumation rates were determined for seven large catchments in the
21 Venezuelan Andes from fission-track analysis of detrital apatite. A quantitative comparison
22 between eight new detrital apatite fission-track (AFT) age distributions presented here and
23 previously published bedrock AFT age patterns shows that detrital AFT ages can be used for
24 predicting exhumation patterns across the mountain belt. Catchment-averaged exhumation
25 rates estimated from the raw data range from 0.48±0.02 to 0.80±0.26 km Myr^{-1}. Accounting
26 for variable sediment yield and assuming that short-term sediment production rates scale with
27 long-term exhumation rates, these rates vary from 0.33±0.07 to 0.48±0.08 km Myr^{-1}. No
28 variation in rates is observed between the northwestern and southeastern flanks of the
29 mountain belt, despite a threefold increase in precipitation from the northwest to the
30 southeast. Long-term exhumation rates are strongly correlated with relief in the different
31 catchments, but no or negative correlations exist with precipitation data or present-day erosion
32 indexes, while the correlation with seismic energy released by earthquakes is weak to
33 moderate. This lack of correlation may be caused by the insufficient temporal range of the
34 available precipitation and seismicity data, and the different time scales involved in the
35 comparison. Long-term exhumation rates are, however, strongly correlated with seismic strain
36 rates (which take the temporal earthquake magnitude-frequency scaling into account),
37 suggesting that the moderate correlation with seismic energy is indeed related to the different
38 timescales and that tectonic control on exhumation is significant. In contrast, given that
39 precipitation patterns in the Venezuelan Andes should have been installed during Miocene

40 times, we suggest that decoupling of relief and exhumation from present-day climate explains
41 the lack of correlation between exhumation and precipitation.
42
43 **Keywords:** Venezuelan Andes, detrital apatite fission-track, exhumation, erosion rates, relief,
44 climate.
45
46 **1. INTRODUCTION**
47
48 The relative importance of tectonic and climatic control on relief development and
49 exhumation in mountain belts remains strongly debated (e.g., Molnar and England, 1990;
50 Burbank et al., 2003; Reiners et al., 2003; Strecker et al., 2009; Champagnac et al., 2012).
51 Problems limiting our ability to discriminate between the driving forces for the development
52 of topography and erosion include the limited temporal precision with which variations in
53 exhumation rate, climate and tectonics can be resolved and compared (e.g., Whipple, 2009),
54 and the different temporal scales for which we have records of these processes (Burbank et al.,
55 2003; Reiners et al., 2003; Vernon et al., 2009). While thermochronologic data record
56 denudation on million-year timescales, seismicity (arguably a proxy for the intensity of at
57 least brittle tectonics) and precipitation records (an admittedly reductionist climate descriptor)
58 generally do not go back more than a few decades. Nevertheless, the comparison of spatial
59 patterns of long-term exhumation rates and short-term seismicity and precipitation may
60 provide some first-order insights into the processes driving exhumation, even in the absence
61 of strong spatial correlations (Finlayson et al., 2002; Dadson et al., 2003; Koons, 2009;
62 Vernon et al., 2009).
63
64 The Andes are important in the discussion on climate versus tectonic controls on topography
65 and exhumation in mountain belts because of the obvious link between laterally varying

topographic characteristics and climatic zonation (e.g., Montgomery et al., 2001; Lamb and Davies, 2003), as well as the strong asymmetry in orographic precipitation associated with this orogen (e.g., Bookhagen and Strecker, 2008). While many studies have concentrated on the southern and central Andes (e.g., Strecker et al., 2007; Farías et al., 2008; Thomson et al., 2010), attention has recently also focused on the northern Andes. Mora et al. (2008), for instance, describe strongly asymmetric deformation and exhumation patterns in the eastern Colombian Andes, which they link to the strong NW-SE precipitation gradient across this part of the mountain belt. In contrast, Mora et al. (2009) and Parra et al. (2009) argue for a strong control of inherited crustal structure on spatio-temporal patterns of exhumation and relief production.

In this study, we present new detrital apatite fission-track (AFT) data from eight river catchments in the Venezuelan Andes, the north-easternmost extension of the Northern Andes. We compare the detrital AFT data to available bedrock AFT data of the Venezuelan Andes (Kohn et al., 1984; Bermúdez et al., 2010, 2011) in order to test whether they faithfully record exhumation in the catchments (e.g., Ruhl and Hodges, 2005; Brewer et al., 2006) and to spatially integrate the still relatively sparse *in-situ* data. The objective of this study is to examine the relative control of climate and tectonics on exhumation and relief development in the Venezuelan Andes. For this purpose, long-term exhumation rates derived from the detrital thermochronology data are compared to present-day relief, precipitation rates, seismic energy release, seismic strain rate and short-term erosion potential predicted from the average stream power of individual drainages.

2. GEOLOGIC SETTING

The Venezuelan Andes were formed by oblique convergence between the continental Maracaibo block and the South American plate, driven by eastward movement of the Caribbean plate (Fig. 1A; Case et al., 1990). The orogen is characterized by high seismicity and spatially variable exhumation since Miocene times, as recorded by AFT thermochronology data (Kohn et al., 1984; Bermúdez et al., 2010, 2011). The structure of the Venezuelan Andes is controlled by reactivated faults that delineate individual tectonic blocks (Fig. 1B). These faults were inherited from Early Mesozoic rifting, and possibly from earlier orogenesis (Aleman and Ramos, 2000; Pindell and Kennan, 2001). Bermúdez et al. (2010) defined at least seven tectonic blocks with contrasting exhumation and cooling histories, separated by major strike-slip and thrust faults. The orogen is bounded by two seismically active thrust belts to the northwest and southeast (Coletta et al., 1997). The most important strike-slip fault systems are the right-lateral Boconó, Central-Sur Andino and Caparo faults and the left-lateral Icotea, Valera, and Burbusay or Carache fault systems (Fig. 1B). The Boconó fault zone extends from the border with Colombia for more than 500 kilometers to the northeast (Fig. 1) and divides the Venezuelan Andes symmetrically in its central part into two separate chains; the Sierra La Culata to the northwest and the Sierra Nevada to the southeast. These two blocks cooled rapidly but diachronously during the late Miocene–Pliocene (Kohn et al., 1984; Bermúdez et al., 2011). In contrast, the Caparo and Trujillo blocks (Fig. 1B), at the southwestern and northeastern ends of the Venezuelan Andes respectively, experienced slow cooling from the late Oligocene - late Miocene onward (Bermúdez et al., 2010). Both these blocks are dominated by Paleozoic and Mesozoic sedimentary rocks, whereas Proterozoic to Paleozoic gneisses and granites are exposed in the core of the mountain belt, in the Sierra Nevada and Sierra La Culata ranges. This crystalline basement is covered by

115 Cenozoic sedimentary rocks of the Maracaibo and Barinas foreland basins to the north and
116 south, respectively (Fig. 1).
117
118 **3. DETRITAL APATITE FISSION-TRACK THERMOCHRONOLOGY**
119
120 Thermochronology of detrital minerals allows quantifying cooling rates and exhumation
121 processes in convergent mountain belts (e.g., Garver et al., 1999; Carter, 2007), providing a
122 complimentary record of the erosional history of a mountain belt with respect to local cooling
123 paths deduced from *in-situ* samples within the orogen (Brandon and Vance, 1992). Detrital
124 thermochronology applied to modern river sediments provides a spatially integrated view of
125 the exhumation history of an entire drainage basin, which may be the only way to characterise
126 exhumation patterns for inaccessible areas.
127
128 **3.1. Data collection and discrimination of age components**
129 We collected samples for detrital AFT thermochronology from eight river catchments
130 draining the Venezuelan Andes. The Coloncito, Tucaní, San Pedro, Agua Viva, and Mimbós
131 rivers drain the northern flank, the Chama and Chejendé rivers drain the central range, and the
132 Santo Domingo River drains the southern flank of this mountain belt (Fig. 2). Samples were
133 collected along active river channel bars at all sites and prepared using standard techniques
134 (cf. Bermúdez et al., 2010). We aimed at dating at least 100 grains per sample in order to
135 attain statistically significant AFT age populations. This objective was attained for 5 out of 8
136 samples (Table 1).
137
138 Because apatites in detrital samples are derived from different sources with variable bedrock
139 ages within a drainage area, the grain-age distribution may contain several grain-age

components (Brandon and Vance, 1992; Garver et al., 1999). Different methods have been proposed for decomposing a fission-track grain age distribution into its age components, the most popular of which has become the binomial peak-fitting method (e.g. Galbraith and Green, 1990; Brandon 1992, 1996). Here, we use this method (as described by Stewart and Brandon, 2004) to decompose the grain-age distributions of our modern river samples. Resulting age peaks are reported in Table 1 and Figure 2. All samples except 1707 from the Tucaní catchment record a Late Miocene (6-10 Ma) age peak, and all except those from the northwestern-most catchments (Agua Viva and Chejendé) also record a Mio-Pliocene (2.5-6 Ma) age peak. Although all samples contain older (15-35 Ma) single-grain ages, only the Santo Domingo, Agua Viva, Tucaní and Chama catchments record an older (Early-Middle Miocene; 14-25 Ma) age peak. The Late Miocene age population is dominant (57 to 100%) in most samples, except for the Santo Domingo and Coloncito catchments where the younger (Mio-Pliocene) age population is larger. In the Tucaní sample, 90% of the grains are grouped in a 5.9±0.7 Ma age peak. The Chejendé River is a tributary of the Agua Viva and drains part of its catchment (Fig. 1); for this reason we merged the detrital data for the corresponding samples (0507 and 0807) and proceed to apply the decomposition of the grain-age distribution as above. The resulting age peaks are very similar to those from the Agua Viva sample alone (Table 1).

Access to the southern flank of the Venezuelan Andes is difficult and our dataset contains only one river draining to the south. The Santo Domingo River sample shows a similar grain-age distribution and peak ages as the rivers that drain to the north (Table 1, Figure 2), although the component ages are slightly older than corresponding age peaks in the other samples.

Although binomial peak fitting provides a convenient means of analyzing detrital thermochronology data, it may mask similarities in age structure between different samples. In order to analyze these, we use the Kolmogorov-Smirnov and Kuiper tests (Conover, 1980) to quantitatively compare the detrital age probability density functions (PDF) for the seven catchments (cf. Supplementary Material; Figure S1 and Table S1). These comparisons indicate that, at a 95% confidence level, the samples from four catchments located in the central part of the Venezuelan Andes (Chama, Tucaní, Santo Domingo and San Pedro) yield a similar detrital age distribution, while the age distributions of the other samples are significantly different from each other.

3.2. Comparison of detrital and bedrock AFT ages

Previous studies have shown that detrital thermochronology faithfully records source-area exhumation in a number of different settings (e.g. Bernet et al., 2004; Ruhl and Hodges, 2005; Brewer et al., 2006). Here, we compare our detrital AFT grain-age distributions of an individual drainage to previously published bedrock AFT ages. We analyse the Chama catchment, as it is the only one within the Venezuelan Andes for which sufficient *in-situ* data (Kohn et al. 1984; Bermúdez et al., 2011) are currently available to derive a reliable bedrock age map.

Several authors (Stock et al., 2006; Vermeesch, 2007; McPhillips and Brandon, 2010) have developed quantitative methods for comparing bedrock and detrital age patterns. We adopt the approach described by Vermeesch (2007), randomly sampling a number of ages equal to the number of single-grain ages in the detrital sample from the interpolated bedrock age map (see Glotzbach et al., in review for details). This method has the advantage that it takes into account Poisson-distributed measurement uncertainties. We sample the bedrock age

190 distribution and construct the predicted age probability-density function (PDF) and
191 cumulative-density function (CDF) 1000 times (Fig. 3a). We then use the Kolmogorov-
192 Smirnov (KS) (Conover, 1980) and Kuiper equality tests (Ruhl and Hodges, 2005) to compare
193 the predicted AFT CDFs and PDFs with the detrital AFT data. Additional simulations (5000;
194 10000) do not change the statistical results of our comparison. The resulting average *p*-values
195 show that the inferred bedrock age distribution is significantly different from the detrital age
196 distribution at the 95% confidence level; all simulations fail the Kuiper test and the vast
197 majority also fail the KS test.
198
199 There are several possible reasons for this discrepancy. First, we do not take into account
200 potential variations in apatite content for different lithologies in the catchment, whereas this
201 may strongly influence the detrital age distribution (e.g., Tranel et al., 2011). However, (1) we
202 have no information on the relative apatite abundance in different rock types of the
203 Venezuelan Andes, (2) the sampled Chama catchment is mainly underlain by relatively
204 homogeneous Precambrian basement rocks (see Chama River in Fig. 1B).
205
206 Another possibility is that the catchment is not currently eroding at a uniform rate, which is an
207 inherent assumption when randomly picking ages from the interpolated bedrock age
208 distribution. It is relatively simple to weight the bedrock age distribution according to a model
209 of inferred present-day erosion rates (Vermeesch, 2007; McPhillips and Brandon, 2010;
210 Glotzbach et al., in review). Here we assume that the short-term erosion rates in the catchment
211 are coupled to the long-term exhumation rates, which can be estimated from the AFT ages
212 using a simple 1D thermal model (cf. next section). We thus resample the interpolated
213 bedrock age distribution, letting the probability of sampling any particular age be determined
214 by the long-term exhumation rate associated with that age, relative to the average long-term

exhumation rate of the catchment. The resulting predicted CDF's/PDF's compare very favourably to the observed detrital AFT age distribution (Fig. 3B); both the KS and Kuiper tests suggest the two distributions are similar at the 95% confidence level.

We conclude from the above comparisons that the detrital AFT age distributions provide a reliable estimate of *in-situ* bedrock ages in the sampled catchments when weighted by their associated long-term exhumation rates, implying that the apatite yield of the catchment (as recorded by our detrital samples) is controlled by the long-term exhumation rates.

3.3. Long-term exhumation rates

The detrital age distributions can be used to provide predictions of average long-term exhumation rates of individual drainages, which can be compared to potential tectonic or climatic control parameters. We employ a simple 1-D steady-state thermal model developed by Brandon et al. (1998; see also Ehlers, 2005; Reiners and Brandon, 2006) to convert detrital AFT ages to exhumation rates. As this model does not take either transient thermal effects (e.g. Rahl et al., 2007) or the 3-D effects of topography (e.g., Whipp et al., 2009) into account, predicted exhumation rates should be considered as first-order estimates. Parameters used for these calculations are a surface temperature of 25°C, layer thickness to constant temperature of 40 km, thermal diffusivity of 25 km^2 My^{-1}, heat production of 10 °C My^{-1} and a temperature at the base of the layer of 700 °C (see Bermúdez et al., 2011 for details). The last two values were constrained by inverse modeling of age-elevation relationships in the central Venezuelan Andes (Bermúdez et al., 2011) and imply a pre-exhumation surface geothermal gradient close to 25 °C km^{-1}. The model iteratively calculates an exhumation rate (ε), cooling rate, closure-temperature (T_c) and -depth (z_c) from the AFT ages, using the Dodson (1973)

239 equation to solve for the closure temperature of the AFT thermochronometer and a steady-
240 state thermal structure to relate this to the closure depth.
241
242 For each detrital sample, we use the above procedure to translate single-grain ages into
243 exhumation rates, which we then combine to predict a catchment-wide average long-term
244 exhumation (ε_T) rate as:

245 $$\varepsilon_T = \frac{1}{N}\sum_{j=1}^{N}\varepsilon_j \quad (1)$$

246 where ε_j is the exhumation rate inferred for grain j and N is the total number of grains in the
247 detrital sample. In order to include the expected effect that rapidly exhuming areas of a
248 catchment will contribute more sediment (and thus more datable apatite grains), as indicated
249 by the comparison of bedrock and detrital age distributions in the previous section, we also
250 calculate a weighted long-term catchment-averaged exhumation rate $(\varepsilon_T)_w$:

251 $$\left(\varepsilon_T\right)_w = \frac{N}{\sum_{j=1}^{N}\frac{1}{\varepsilon_j}} \quad (2)$$

252 Results are reported in Table 2. Catchment-averaged exhumation rates vary between
253 0.48±0.02 km Myr^{-1} for the Santo Domingo and 0.80±0.26 km Myr^{-1} for the Mimbós
254 catchments. As expected, weighted-average rates are lower, and all weighted long-term
255 exhumation rates in the Central Venezuelan Andes overlap within error, varying between
256 0.33±0.07 (Agua Viva-Chejendé) and 0.48±0.08 (Coloncito) km Myr^{-1}. The northeastern
257 Agua Viva/Chejendé catchment shows the lowest long-term exhumation rates (< 0.35 km
258 Myr^{-1}). The central Chama and Santo Domingo catchments show intermediate rates (0.35-
259 0.40 km Myr^{-1}) and the catchments located on the northwestern flank of the range show the
260 highest exhumation rates (> 0.40 km Myr^{-1}). In the following discussion, we will focus on the

261 weighted-average catchment exhumation rates, which we consider to be the most reliable
262 estimates.
263
264 **4. POTENTIAL CONTROLLING PARAMETERS**
265
266 In order to explore the potential topographic, tectonic or climatic controls on the exhumation
267 rates determined above, we derive quantitative measures for these controls (relief,
268 precipitation, seismicity, stream power) in the following sections.
269
270 **4.1. Elevation and Relief**
271 The Venezuelan Andes rise from sea level at Lake Maracaibo, to the north of the mountain
272 belt, to close to 5000 m elevation at Pico Bolívar in the Sierra Nevada Block (Fig. 1B). This
273 part of the Andes most probably emerged as an orographic barrier at about 8 Ma (Hoorn et
274 al., 1995; Bermúdez et al., 2011). The central Sierra Nevada and Sierra la Culata ranges (Fig.
275 1C) include more than 60 peaks with elevations of 4300 m and above (Fig 4A). These highest
276 parts of the Venezuelan Andes were glaciated during the Quaternary. Moraines of the Last
277 Glacial Maximum are encountered at 3400-3600 m elevation (Schubert, 1984), with older
278 moraines occurring at elevations several hundred meters lower. The mean elevation of the
279 range is significantly lower to the northeast and southwest, varying between 1160 and 1695 m
280 (Bermúdez et al., 2010).
281
282 Relief was calculated as the maximum elevation difference within a variable radius, between
283 1 and 15 km, for every pixel in the digital elevation model (e.g., Montgomery and Brandon,
284 2002). There is a power-law relationship between average relief of the different catchments
285 and the radius at which it was calculated, with scaling exponents around 0.5-0.6, characteristic

286 for low-latitude mountain belts (Champagnac et al., 2012). The present-day relief of the
287 Venezuelan Andes for a 5-km radius is shown in Figure 4A. Highest relief values of close to
288 3500 m are found along the central Chama River valley, which follows the Boconó fault.
289 Other areas of high relief are located on the northwestern and southeastern flanks of the
290 mountain belt. Relief is much lower within the central Sierra Nevada and Sierra la Culata
291 ranges and in the Caparo and Trujillo blocks in the southwest and northeast of the Venezuelan
292 Andes (Fig. 1B, 4A). The former are characterized by extensive low-relief summit surfaces
293 that show widespread evidence for glacial bevelling through cirque retreat (e.g., Mitchell and
294 Montgomery, 2006; Foster et al., 2008), whereas the latter show subdued relief at lower mean
295 elevations with widespread soil mantling of slopes.
296
297 **4.2 Precipitation**
298 The topography of the Venezuelan Andes generates a well-developed orographic precipitation
299 pattern. Moist air masses from equatorial South America in the south need to rise in order to
300 cross the Venezuelan Andes to the north, causing heavy precipitation on its southern flank,
301 whereas the centre and northern flank of the belt are more arid. It has been proposed that the
302 present-day precipitation and drainage system of the Venezuelan Andes started developing at
303 about 8 Ma, in response to tectonically driven surface uplift (Hoorn et al., 1995; Bermúdez et
304 al., 2011). We have used precipitation data from 30 meteorological stations in and around the
305 Venezuelan Andes to elaborate a mean annual precipitation map for the past twenty years.
306 Although these measurements do not record snowfall as accurately as rainfall, the vast
307 majority of precipitation is rainfall in the low-latitude Venezuelan Andes. The database was
308 compiled from different sources: (1) NOAA World Temperature – Precipitation dataset
309 (http://bonnet19.cs.qc.edu:7778/pls/rschdata/rd_start.main); (2) published data (Stansell et al.,
310 2006; Naranjo & Duque, 2004); (3) Bio-climatic net stations of Mérida

311 (http://www.cecalc.ula.ve/redbc/colecciones/colecciones_datos.html); and (4) data provided
312 by Gerard Kopp (pers. comm.) of the Institute for Meteorology and Climate Research,
313 University of Karlsruhe (Germany) for the Mérida Atmospheric Research Station at Pico
314 Espejo (MARS). The present-day precipitation map shown in Figure 4B was compiled from
315 these data using nearest-neighbor interpolation (Arya et al., 1998) and highlights the strong
316 precipitation gradient between the northern and southern flanks of the Venezuelan Andes,
317 with precipitation ranging from 1.6 to 3.4 m yr^{-1} on the southern flank as opposed to 0.09-1.1
318 m yr^{-1} on the northern flank. A particular feature is the arid patch that expands into the orogen
319 between El Vigía and Mérida: hot dry winds from the north exploit the Chama River valley to
320 penetrate deep into the orogen, generating a unique arid climate in this area (Fig. 4B). A
321 remotely sensed (TRMM) precipitation dataset synthesized by Bookhagen and Strecker
322 (2008) shows overall similar patterns, both qualitatively and quantitatively.
323
324 **4.3. Seismicity**
325 Historical and instrumental seismicity in the Venezuelan Andes is strongly concentrated along
326 the Boconó fault system. Smaller seismic events are scattered within a band of several tens of
327 km width adjacent to this fault zone, indicating that many of the fault branches are also active
328 (Fig. 5A). However, most of the seismicity occurs along the main trace of the fault at an
329 average depth of about 15 km. Larger seismic events tend to occur at greater depth to the
330 northwest (Lake Maracaibo basin) and southeast (Barinas basin) of the surface trace of the
331 Boconó fault, reaching more than 40 km depth (Dewey, 1972, Niu et al., 2007). A seismic
332 zone of intermediate depth (~160 km) occurs towards the southwestern boundary of the
333 Venezuelan Andes and continues below the Eastern Cordillera of Colombia. This significant
334 concentration of events is known as the Bucaramanga seismic nest (Schneider et al, 1987) and
335 occurs within the subducted Caribbean slab below northern South America (van der Hilst and

336 Mann, 1994). More scattered, but relatively high magnitude (M > 5) earthquakes are
337 associated with the north-south oriented Icotea, Valera and Burbusay fault systems to the
338 north of the Venezuelan Andes (Fig. 5A).
339
340 Focal mechanisms suggest predominantly right-lateral faulting along the Boconó fault, left-
341 lateral faulting along the north-south trending faults to the north of the Venezuelan Andes,
342 and orthogonal thrusting along the northwest and southeast foreland fold-and-thrust belts
343 (Colmenares and Zoback, 2003; Corredor, 2003; Cortés and Angelier, 2005). These focal
344 mechanisms indicate a compressional stress regime with σ_1 oriented approximately WNW-
345 ESE across the central Venezuelan Andes, evolving toward a strike-slip regime with a NW-
346 SE directed σ_1 axis to the northeast. Studies of active tectonic landforms in the Venezuelan
347 Andes, together with regional tectonic reconstructions, suggest that the current tectonic
348 regime was installed during Pliocene-Quaternary times (Backé et al., 2006; Egbue and
349 Kellogg, 2010).
350
351 In order to quantify the effects of seismicity across the Venezuelan Andes, we compiled a
352 seismicity record over the last century (from January 1911 to January 2011), using data
353 available from the digital library of the Geophysics Laboratory of Universidad de Los Andes,
354 Mérida (http://lgula.ciens.ula.ve/) and data provided by the Venezuelan Foundation for
355 Seismological Investigation (FUNVISIS; http://www.funvisis.gob.ve). The data were filtered
356 using two criteria: (1) epicenters of earthquakes located between latitudes 72.25°W - 70.00°W
357 and longitudes 7.75°N - 10.00°N; (2) only data with reported local magnitudes M_l were
358 considered. Figure 5A shows a summary of earthquakes that occurred in the Venezuelan
359 Andes during the last century. We calculated the released seismic energy (Se) from the local
360 magnitudes using the classical expression of Gutenberg and Richter (1954):

$$\log(Se) = bM_l + a \approx 1.5M_l + 4.8 \quad (3)$$

The values of the parameters a and b are estimated by a least-squares fit of cumulative magnitude-frequency relationships constructed from subsamples of the seismic database for each catchment in 0.5º×0.5º cells and are equivalent to the intersect and slope, respectively, of the Gutenberg-Richter relationship (Gutenberg and Richter, 1954). Released seismic energy values were cumulated within circles with radius of 25 km around the epicenter of each earthquake. Figure 5B shows the resulting map of seismic energy obtained from this procedure. The rate of seismic energy release is highest in the central Venezuelan Andes (Chama catchment) and decreases toward the northeast and southwest. However, the calculated pattern is strongly affected by the $M_l > 5$ earthquakes that occurred on the Burbusay, Valera and Icotea fault systems.

The record of seismic energy release spans only 100 years, significantly shorter than the return period of major earthquakes in the Venezuelan Andes (300 years for $M \geq 7$ earthquakes; Audemard, 1997). Consequently, the pattern of released seismic energy may be locally underestimated. However, the seismicity records brittle deformation of the upper crust; the spatial distribution and frequency of earthquakes are intuitively related to the rate of brittle deformation (e.g. Holt et al., 2000). Thus, we can use the compiled seismic database to estimate the present-day distribution of brittle strain rate and extrapolate the total amount of seismic strain over timescales longer than the observation interval, using the observed earthquake magnitude-frequency (Gutenberg-Richter) relationship. To achieve this, we use the method described by Braun et al. (2009) and calculate seismic/brittle strain rate as:

$$\varepsilon_H = \left(\frac{1}{2\mu\Delta V\Delta t}\right)\left(\frac{b10^{a+9.1}}{1.5-b}\right)\left(10^{(1.5-b)M_{\max}}\right) \quad (4)$$

384 in which the parameters a and b are defined and calculated as explained above; M_{max} is the
385 maximum observed magnitude; μ is elastic shear modulus; ΔV is the volume of the crust (that
386 is, the moving 0.5º×0.5º cell area multiplied by depth of the maximum magnitude earthquake)
387 in which the earthquakes were observed over a period of time Δt (in this case, Δt = 100 years).
388 The depth of the maximum magnitude earthquakes (33-163 km) generally exceeds the depth
389 of brittle-ductile transition (~15-20 km). Because we are using the seismic strain rate as a
390 proxy for brittle deformation, we recalculated seismic strain rates using only earthquakes with
391 hypocentral depths less than 20 km. However, we did not find any significant differences
392 between the two approaches. The maximum-magnitude bin used in the least-squares fit
393 always had at least one earthquake in it. Cells with a correlation coefficient, $r^2 < 0.95$ (mostly
394 due to an incomplete catalogue) were not considered. In order to check the robustness of the
395 results, we tested the effect of removing the minimum and maximum magnitude bins on the a
396 and b values and the effect of forcing b to be exactly 1, but neither caused the seismic strain
397 rate to change significantly.
398
399 Figure 5C shows the resulting map of seismic/brittle strain rate from subsamples (sliding
400 0.5 × 0.5° cells) of the seismic database for the Venezuelan Andes. The resulting seismic
401 strain-rate map (Fig. 5C) shows maximum deformation occurring in the central and northwest
402 Venezuelan Andes, with a second maximum occurring to the south of the mountain belt in the
403 area of the 2001/12/21, M_w = 5.6 earthquake. Seismic strain rates vary between ~10^{-17} s^{-1} at
404 the northeastern (Agua Viva-Chejendé catchment) and southwestern extremities of the belt,
405 the latter influencing average seismic strain rates in the Chama catchment, and ~10^{-15} s^{-1} in the
406 centre of the belt (Mimbós, San Pedro and Coloncito catchments).
407

408 **4.4 Short-term erosion potential**

409 The long-term exhumation rates estimated from detrital AFT ages can be compared to model
410 predictions of the intensity of short-term erosion using the erosion-index approach of
411 Finlayson et al. (2002). The erosion index (*EI*) can be calculated in different ways as a
412 function of stream power, which is the rate of potential energy expenditure by flowing water
413 and has been used extensively in studies of erosion, sediment transport, and geomorphology
414 as a measure of the erosive power of rivers and streams (Wilson and Gallant, 2000; Wobus et
415 al., 2006). The analysis is based on a prediction of bedrock incision rate as a function of
416 stream power (Finlayson et al., 2002; Tucker and Whipple, 2002):

417 $$e = k\ A^m S^n \tag{5}$$

418 where e is the local incision rate, A is upstream drainage area (used as a proxy of discharge), S
419 is local slope, and m, n and k are constants. The parameter k is mainly related to bedrock
420 erodibility. Given the similar geologic and geographic conditions of the studied catchments
421 and the lack of information on relative erodibility of the different lithologies outcropping in
422 the Venezuelan Andes, we take k to be uniform throughout the study area. Setting k to unity,
423 the predicted erosion index becomes:

424 $$EI = A^m S^n \tag{6}$$

425 Spatial variations in precipitation P can be incorporated into the prediction of EI in order to
426 study their influence on spatial variability of the erosion potential:

427 $$EI_p = \sum\left[\left(A_p\right)P\right]^m S^n \tag{7}$$

428 where (A_p) is the pixel area, P is the local precipitation and the summation sign implies
429 summing the along the flow-lines within the catchment in order to calculate the flow
430 accumulation. We term EI_p the precipitation-modulated erosion index.

431

Different m and n values can be employed in equations (6) and (7), depending on the control of river incision rates by total stream power, stream power per unit channel width or shear stress (Finlayson et al., 2002; Tucker and Whipple, 2002). In the case where incision is controlled by total stream power (TSP), $m = n = 1$. For incision controlled by stream power per unit channel width (USP), $m = 1/2$ and $n = 1$. If incision is controlled by fluvial shear stress (SSP), $m = 1/3$ and $n = 2/3$.

Normalized erosion index maps for the Venezuelan Andes, predicted by the six possible models (TSP, USP, and SSP for uniform or spatially variable precipitation) are shown in Figure 6. These maps emphasize distinct zones of high erosion potential associated with the steepest terrain and largest discharge of the main rivers. If uniform precipitation is considered, the most important zones of high erosion potential of the Venezuelan Andes are located in the central Chama and Santo Domingo valleys, with secondary regions of high erosion potential on both the northern and southern flanks. Consequently, under this assumption the Chama and Santo Domingo rivers, together with the small catchments (Tucaní, San Pedro, Mimbós) on the northwest flank of the orogen, have high relative erosion indexes (whether considering TSP, USP or SSP) with the peripheral Coloncito and Agua Viva-Chejendé River catchments showing lower erosion indexes (Table 2).

When the precipitation data are incorporated in the erosion index predictions, the results differ significantly because of the strong orographic effect (Figure 4B), with maximum erosion potential shifting to the southeastern flank of the mountain belt (Figure 6). In particular, the predicted high relative erosion index in the central Chama River valley disappears when precipitation is taken into account, due to the pronounced aridity of this valley. Consequently, the southeast-draining Santo Domingo catchment is predicted to have the highest relative

457 erosion index (whether considering TSP, USP or SSP), followed by the Chama River
458 catchment. Incorporating spatially variable precipitation lowers the relative erosion index
459 values for the small northwestern Tucaní, San Pedro and Mimbós catchments, which become
460 indistinguishable from those for the peripheral Agua Viva-Chejendé and Coloncito
461 catchments (Table 2).
462
463 **5. DISCUSSION: RELATIONS BETWEEN TECTONICS, CLIMATE AND**
464 **EROSION IN THE VENEZUELAN ANDES**
465
466 Whether long-term exhumation rates in mountain belts are controlled to first order by tectonic
467 or climatic factors remains a matter of debate. Some authors have argued for strong coupling
468 between long-term exhumation and precipitation, for instance for the Central Andes
469 (Montgomery et al., 2001), Washington Cascades (Reiners et al., 2003), while others argued
470 for decoupling between long-term exhumation and precipitation, such as in the central
471 Himalaya (Burbank et al., 2003) or in the European Alps (Vernon et al., 2009). Recently,
472 Mora et al. (2008) have argued for coupling between precipitation and exhumation rates in the
473 Eastern Cordillera of Colombia, which is contiguous to the Venezuelan Andes. Can long-term
474 exhumation rates in the Venezuelan Andes be correlated to present-day precipitation rates? If
475 they are uncorrelated with precipitation, what could be the controlling factor driving
476 exhumation? The underlying question is, how strongly are tectonic and climatic processes
477 coupled and on which timescales? Table 2 summarizes our observations on long-term
478 exhumation, predicted short-term erosion potential and potential controlling factors for the
479 seven studied catchments in the Venezuelan Andes. The challenge lies in comparing
480 exhumation rates over several millions of years, derived from detrital AFT ages, with present-
481 day precipitation or seismicity data that was collected over the past 100 years or less.

In order to gain insight into the potential controls on erosion and exhumation rates in the Venezuelan Andes, we have calculated Pearsonian correlation coefficients between each of the measures reported in Table 2. Table 3 summarizes the results of this analysis. Given that we compare all variables for seven catchments, correlations are statistically significant (at a 95% confidence level) for a Pearson correlation coefficient $r \geq 0.7$.

Figure 7 shows how long-term exhumation rates in the Venezuelan Andes correlate with different potential control parameters (present-day relief, precipitation, seismic energy release, seismic strain rate and stream power). A first observation is the very strong positive correlation ($r = 0.88$) between long-term exhumation rates and relief, implying that the present-day relief of the Venezuelan Andes is adapted to the long-term exhumation rates. The correlation we find here is much stronger than that reported, for instance, in the European Alps (Wittmann et al., 2007; Vernon et al., 2009) or in the San Bernardino Mountains of California (Binnie et al., 2007). The reason for this is probably the comparably lower exhumation rates and relief in the Venezuelan Andes, so that bedrock landsliding on threshold slopes, which tends to decouple relief and exhumation rates (Montgomery and Brandon, 2002) is less important with respect to these other mountain belts. In effect, a large proportion of slopes close to the threshold for landsliding is only encountered in the central Sierra Nevada and Sierra la Culata blocks of the Venezuelan Andes (Bermúdez et al., 2010).

In contrast, long-term exhumation rates appear to be decoupled from present-day precipitation rates; they appear even (weakly) negatively correlated with present-day precipitation (i.e. highest exhumation rates occur on the dry northwest flank of the orogen). Also, whereas short-term erosion indexes (*EI*) are not correlated to long-term exhumation rates for any of the

three models (i.e. TSP, SSP or USP), the correlations become even weaker or negative when spatially variable precipitation rates are taken into account in the calculation of these measures (EI_p). The lack of correlations suggests that the present-day precipitation pattern does not strongly control long-term exhumation rates in the Venezuelan Andes, in contrast to what has been inferred for the contiguous Eastern Cordillera of Colombia (Mora et al., 2008). However, two caveats need to be recalled before concluding from this data that climate and exhumation are decoupled in the Venezuelan Andes. First, the relatively limited spatial extent of our sampled catchments, for which the wet southern flank is clearly under-represented, and second the timescale problem mentioned previously. Considering the first, it is clear that our dataset would benefit from inclusion of additional remote south-flank catchments. As for the problem of comparing measurements on strongly varying timescales, whereas we obviously acknowledge that we cannot readily extrapolate the present-day precipitation measurements several million years into the past, we do note that (1) the Neogene sedimentary record of northern South America suggests that the topographic relief of the Venezuelan Andes, and therefore its associated orographic imprint, has been in place since Late Miocene times (Hoorn et al., 1995; Díaz de Gamero, 1996); and (2) Quaternary glaciations, which may strongly modify erosion patterns in some mountain belts (e.g., Burbank et al., 2003; Gabet et al., 2008; Vernon et al., 2009) have been relatively limited in the Venezuelan Andes (Schubert, 1984; Stansell et al., 2006). It has been suggested, both in the Andes and elsewhere (e.g., Bookhagen et al., 2005; Abbühl et al., 2010), that spatial patterns of erosion are strongly by the occurrence of extreme events, leading to decoupling between patterns of erosion and present-day average climate. This could be the case in the Venezuelan Andes, but sufficient resolution in the regional climate record to address this question is currently lacking.

531 In order to assess potential tectonic controls on long-term exhumation rates, we use
532 cumulative seismic energy release and seismic strain rate as proxies for tectonic forcing
533 (Tables 2 and 3). We estimate the cumulative seismic energy released within the different
534 catchment in two different ways: by averaging the values of Figure 5B within each catchment,
535 or by simply summing the seismic energy released by each earthquake within the catchment
536 boundaries and normalising by catchment area. The difference between the two methods is the
537 extent to which earthquakes occurring outside the catchment boundaries are taken into
538 account.
539
540 The inferred seismic energy release correlates weakly to moderately with either catchment-
541 averaged exhumation rate or 10 km-radius relief, with *r*-values varying between 0.40 and 0.64
542 (Table 3). As noted previously, the pattern of seismic energy release is strongly controlled by
543 large ($M_l > 5$) strike-slip earthquakes located outside the Venezuelan Andes, which contribute
544 significantly to accumulated seismic energy in the low-exhumation Agua Viva-Chejendé
545 catchment for instance. The seismic energy release only integrates a century of data and,
546 similar to the precipitation records, may therefore not be directly comparable to long-term
547 exhumation rates and relief. However, there is very little correlation either between measures
548 of seismic energy release and stream-power based erosion indexes, suggesting that short-term
549 erosion rates (if these are correctly predicted by the stream-power models) are decoupled from
550 seismic energy release.
551
552 In contrast to the pattern of released seismic energy, the inferred seismic strain rate correlates
553 very strongly with both catchment-averaged exhumation rates (r = 0.81) and 10 km-radius
554 relief (r = 0.85). Catchments on the northwest flank of the orogen that show the largest
555 seismic strain rates (Mimbós, San Pedro, Coloncito; $\sim 10^{-15}$ s^{-1}) are also characterized by the

556 highest relief (> 1650 m) and exhumation rates (> 0.4 km Myr^{-1}). In contrast, the northwestern
557 Agua Viva-Chejendé catchment, which has the lowest relief and exhumation rates, also shows
558 very low seismic strain rates (2.5×10^{-17} s^{-1}).
559
560 Our data thus suggest that active tectonic deformation of the Venezuelan Andes provides a
561 much stronger control on long-term exhumation rates throughout the orogen than the pattern
562 of precipitation. It also suggests that the widely used stream-power based erosion potential
563 does not adequately model erosion rates throughout the mountain belt. The reason for this
564 may be that the simple stream-power expression does not take into account the effects of
565 sediment flux, stochasticity of discharge and incision thresholds (e.g., Whipple, 2004; Lague,
566 2010). We have previously suggested an overall tectonic control on relief and exhumation
567 rates in the Venezuelan Andes as the orogen can be divided in fault-bounded blocks that each
568 have their characteristic relief and exhumation history (Bermúdez et al., 2010), as also
569 observed in other obliquely convergent mountain belts (e.g., Spotila et al., 2007). It would be
570 interesting to map out erosion rates throughout the Venezuelan Andes using cosmogenic
571 nuclides in stream sediments in order to analyse whether the same patterns emerge on shorter
572 time scales.
573
574 **6. CONCLUSIONS**
575
576 Detrital AFT analysis of modern river sediment provides an efficient tool for studying long-
577 term exhumation rates in complex areas with difficult access, such as the Venezuelan Andes.
578 We have shown that the technique efficiently records average catchment-wide long-term
579 exhumation rates when compared to *in-situ* samples. The detrital AFT ages of seven major
580 catchments of the Venezuelan Andes reproduce and extrapolate the exhumation patterns

581 reported by Bermúdez et al. (2010; 2011) and can thus be used to infer exhumation rates in
582 areas where *in-situ* data is absent. Our results suggest that using weighted average exhumation
583 rates, in order to include the effect that rapidly exhuming areas of a catchment have higher
584 sediment yields improves both the fit to observed detrital age distributions and the
585 correlations with potential control parameters.
586
587 Catchment-averaged long-term exhumation rates in the Venezuelan Andes are fairly constant
588 at 0.31-0.48 km Myr^{-1}. Rates are higher (>0.4 km Myr^{-1}) on the northwestern flank of the
589 mountain belt (Mimbós, San Pedro, Tucani and Coloncito rivers), whereas they are lowest
590 (0.31 km Myr^{-1}) in the northeastern Agua Viva-Chejendé catchment. The large Chama and
591 Santo Domingo catchments draining the central Venezuelan Andes show intermediate rates of
592 0.37-0.38 km Myr^{-1}. Average exhumation rates correlate very well with relief of the
593 catchments as well as with seismic strain rates, but correlations with both stream-power based
594 predictions of short-term erosion potential and precipitation are weak or negative.
595
596 The lack of correlation between long-term exhumation rates and relief, on the one hand, and
597 precipitation on the other suggests that either precipitation is not the main controlling factor
598 for driving exhumation and relief development in the Venezuelan Andes, or that the short-
599 term record of present-day precipitation is not representative of long-term average values.
600 Alternatively, erosion may be effectively controlled by extreme climate events that are not
601 captured by the record. A moderate correlation with seismic energy release indicates that the
602 100-year seismic record does not fully capture the current deformation, because of the long
603 recurrence time of large seismic events. However, we show that calculating the seismic strain
604 rate and its extrapolation over geologic time is feasible and allows studying relationships
605 between long-term exhumation rate, relief and tectonics. Our study suggests that the climatic

606 control on exhumation rates in the active orogens of northern South America may have been
607 overstated. Climatic variations appear to only have a second-order control on relief, erosion,
608 and long-term exhumation rates, as has been suggested elsewhere (e.g. Riebe et al., 2001a,b;
609 Kirchner et al., 2001).
610
611 **ACKNOWLEDGEMENTS**
612 This study was supported by the CDCH de la Universidad Central de Venezuela (UCV),
613 Project Number PI 08-00-6219-2006 and ECOS-Nord project V08U01. We thank Juan Flores
614 and Antonio León for support during fieldwork. We acknowledge Dr. Gerhard Kopp of the
615 Institute for Meteorology and Climate Research, University of Karlsruhe, Germany, for
616 providing the meteorological data of the Mérida Atmospheric Research Station for Pico
617 Espejo (MARS). María Elena Naranjo of the Universidad de Los Andes (ULA) provided
618 precipitation data of the following stations: Páramo de Mucuchies, Páramo Pico El Aguila,
619 Los Plantíos, Mucubají, Valle Grande and Tabay. FUNVISIS provided access to the
620 seismicity data. Finally, we thank Jean Braun and Christoph Glotzbach for discussion and
621 assistance during the writing of this manuscript, and Bodo Bookhagen and an anonymous
622 reviewer for constructive comments.
623
624 **REFERENCES CITED**
625
626 Abbühl, L.M., Norton, K.P., Schlunegger, F., Kracht, O., Aldahan, A., and Possnert, G., 2010,
627 El Niño forcing on ^{10}Be-based surface denudation rates in the northwestern Peruvian
628 Andes?: Geomorphology, v. 123, p. 257-268, doi: 10.1016/j.geomorph.2010.07.017.
629 Aleman, A., and Ramos, V.A., 2000, Northern Andes, in Cordani, U.G., Milani, E.J., Thomaz
630 Filho, A., and Campos, D.A., eds., Tectonic Evolution of South America: Rio de
631 Janeiro, Companhia de Pesquisa de Recursos Minerais / Serviço Geológico do Brasil,
632 p. 453-480.

633 Arya, S., Mount, D.M., Netanyahu, N.S., Silverman, R., and Wu, A., 1998, An optimal
634 algorithm for approximate nearest neighbor searching in fixed dimensions: Journal of
635 the Association for Computing Machinery,, v. 45, p. 891–923.
636 Audemard, F.A., 1997, Holocene and historical earthquakes on the Boconó fault system,
637 southern Venezuelan Andes: Trench confirmation: Journal of Geodynamics, v. 24, p.
638 155–167.
639 Audemard, F.A., Machette, M.N., Cox, J.W., Dart, R.L and Haller, K.M., 2000, Map and
640 Database of Quaternary Faults in Venezuela and its Offshore Regions: USGS Open-
641 File Report 00–018 (paper edition).
642 Backé, G., Dhont, D., and Hervouët, Y., 2006, Spatial and temporal relationships between
643 compression, strike-slip and extension in the Central Venezuelan Andes: Clues for
644 Plio-Quaternary tectonic escape: Tectonophysics, v. 425, p. 25–53.
645 Bermúdez, M.A., Kohn, B.P., van der Beek, P.A., Bernet, M., O'Sullivan, P.B and Shagam,
646 R., 2010, Spatial and temporal patterns of exhumation across the Venezuelan Andes:
647 Implications for Cenozoic Caribbean geodynamics: Tectonics, v. 29, TC5009,
648 doi:10.1029/2009TC002635.
649 Bermúdez, M.A., van der Beek, P., and Bernet, M., 2011, Asynchronous Miocene-Pliocene
650 exhumation of the central Venezuelan Andes: Geology, v. 39, p. 139–142.
651 Bernet, M., Brandon, M.T., Garver, J.I. and Molitor, B., 2004, Fundamentals of detrital zircon
652 fission-track analysis for provenance and exhumation studies with examples from the
653 European Alps: Geological Society of America Special Paper, v. 378, p. 25–36.
654 Binnie, S.A., Phillips, W.M., Summerfield, M.A. and Fifield, L.K., 2007, Tectonic uplift,
655 threshold hillslopes, and denudation rates in a developing mountain range: Geology v.
656 35, p. 743–746.
657 Bookhagen, B., Thiede, R.C., and Strecker, M.R., 2005, Late Quaternary intensified monsoon
658 phases control landscape evolution in the northwest Himalaya: Geology, v. 33, p. 149-
659 152, doi: 10.1130/g20982.1.
660 Bookhagen, B. and Strecker, M.R., 2008, Orographic barriers, high-resolution TRMM
661 precipitation, and relief variations along the eastern Andes: Geophysical Research
662 Letters, v. 35, L06403, doi: 10.1029/2007GL032011.
663 Brandon, M.T., 1992, Decomposition of fission-track grain-age distributions: American
664 Journal of Science, v. 292, p. 535–564.
665 Brandon, M.T., 1996, Probability density plots for fission-track grain age distributions:
666 Radiation Measurements, v. 26, p. 663–676.

667 Brandon, M.T., and Vance, J.A., 1992, Tectonic evolution of the Cenozoic Olympic
668 subduction complex, Washington State, as deduced from fission track ages for detrital
669 zircons: American Journal of Science, v. 292, p. 565–636.
670 Brandon, M.T., Roden-Tice, M.K., and Garver, J.I., 1998, Late Cenozoic exhumation of the
671 Cascadia accretionary wedge in the Olympic Mountains, northwest Washington State:
672 Geological Society of America Bulletin, v. 110, p. 985–1009.
673 Braun, J., Burbidge, D.R., Gesto, F.N., Sandiford, M., Gleadow, A.J.W., Kohn, B.P., and
674 Cummins, P.R., 2009, Constraints on the current rate of deformation and surface uplift
675 of the Australian Continent from a new seismic database and low-T
676 thermochronological data: Australian Journal of Earth Sciences, v. 56, p. 99–110.
677 Brewer, I.D., Burbank, D.W. and Hodges, K.V., 2006, Downstream development of a detrital
678 cooling-age signal: Geological Society of America Special Paper, v. 398, p. 321–338.
679 Burbank, D.W., Blythe, A.E., Putkonen, J., Pratt-Sitaula, B., Gabet, E., Oskin, M., Barros, A.,
680 and Ojha, T.P., 2003, Decoupling of erosion and precipitation in the Himalayas:
681 Nature, v. 426, p. 652–655.
682 Carter, A., 2007, Heavy minerals and detrital fission-track thermochronology: Developments
683 in Sedimentology, v. 58, p. 851–868.
684 Case, J.E., Shagam, R. and Giegengack, R.F., 1990, Geology of the Northern Andes; an
685 overview: The Geology of North America, v. H, p. 177–200.
686 Cediel, F., Shaw, R.P., and Cáceres, C., 2003, Tectonic assembly of the Northern Andean
687 Block: American Association of Petroleum Geologists Bulletin, v. 79, p. 815–848.
688 Champagnac, J.-D., Molnar, P., Sue, C. and Herman, F., 2012, Tectonics, climate, and
689 mountain topography: Journal of Geophysical Research, v. 117, B02403, doi:
690 10.1029/2011jb008348.
691 Colletta, B., Roure, F., De Toni, B., Loureiro, D., Passalacqua, H., and Gou, Y., 1997,
692 Tectonic inheritance, crustal architecture, and contrasting structural styles in the
693 Venezuela Andes: Tectonics, v. 16, p. 777–794, doi: 10.1029/97TC01659.
694 Colmenares, L., and Zoback, M.D., 2003, Stress field and seismotectonics of northern South
695 America: Geology, v. 31, p. 721–724.
696 Conover, W. J., 1980, Practical Nonparametric Statistics: 2nd ed. Wiley, New York, 493 pp.
697 Corredor, F., 2003, Seismic strain rates and distributed continental deformation in the
698 northern Andes and three-dimensional seismotectonics of northwestern South
699 America: Tectonophysics, v. 372, p. 147–166.

700 Cortés, M., and Angelier, J., 2005, Current states of stress in the northern Andes as indicated
701 by focal mechanisms of earthquakes: Tectonophysics, v. 403, p. 29–58.
702 Dadson S.J., Hovius N., Chen H., Dade W.B., Hsieh M.-L., Willett S.D., Hu J.-C., Horng M.-
703 J., Chen M.-C., Stark C.P., Lague D., and Lin J.-C. 2003, Links between erosion,
704 runoff variability and seismicity in the Taiwan orogen: Nature, v. 426, p. 648–651,
705 doi: 10.1038/nature02150.
706 Dewey, J.W., 1972, Seismicity and tectonics of western Venezuela: Bull. Seism. Soc.
707 America, v. 62, p. 1711–1751.
708 Díaz de Gamero, M.L., 1996, The changing course of the Orinoco River during the Neogene:
709 a review: Palaeogeography, Palaeoclimatology, Palaeoecology, v. 123, p. 385–402.
710 Dodson, M.H., 1973, Closure temperature in cooling geochronological and petrological
711 systems: Contributions to Mineral Petrology, v. 40, p. 259–274.
712 Egbue, O. and Kellogg, J., 2010, Pleistocene to Present North Andean "escape":
713 Tectonophysics, v. 489, p. 248–257, doi: 10.1016/j.tecto.2010.04.021.
714 Ehlers, T. A., 2005, Crustal thermal processes and the interpretation of thermochronometer
715 data: in T. Ehlers and P. W. Reiners (Eds.), Low Temperature Thermochronometry:
716 Techniques, Interpretations, and Applications: Reviews in Mineralogy and
717 Geochemistry, v. 58, p. 315–350.
718 Farías, M., Charrier, R., Carretier, S., Martinod, J., Fock, A., Campbell, D., Cáceres, J., and
719 Comte, D., 2008, Late Miocene high and rapid surface uplift and its erosional response
720 in the Andes of central Chile (33°–35°S): Tectonics, v. 27, TC1005, doi:
721 10.1029/2006TC002046.
722 Finlayson, D.P., Montgomery, D.R., and Hallet B., 2002, Spatial coincidence of rapid inferred
723 erosion with toung metamorphic massifs in the Himalayas: Geology, v. 30, p. 219–
724 222.
725 Foster, D., Brocklehurst, S.H. and Gawthorpe, R.L., 2008, Small valley glaciers and the
726 effectiveness of the glacial buzzsaw in the northern Basin and Range, USA:
727 Geomorphology, v. 102, p. 624–639, doi: 10.1016/j.geomorph.2008.06.009.
728 Gabet, E.J., Burbank, D.W., Pratt-Sitaula, B., Putkonen, J. and Bookhagen, B., 2008, Modern
729 erosion rates in the High Himalayas of Nepal: Earth and Planetary Science Letters, v.
730 267, 482–494.
731 Garver, J.I,, Brandon, M.T,, Roden-Tice, M.K,, Kamp, P.J.J., 1999, Exhumation history of
732 orogenic highlands determined by detrital fission track thermochronology: Geological
733 Society of London, Special Publications, v. 154, p. 283–304.

734 Glotzbach, C., van der Beek, P.A., and Spiegel, C., 2011, Episodic exhumation and relief
735 growth in the Mont Blanc massif, Western Alps from numerical modelling of
736 thermochronology data: Earth and Planetary Science Letters, v. 304, p. 417–430.
737 Glotzbach, C., van der Beek, P.A., Carcaillet, J., and Delunel, R., in review, Deciphering the
738 driving forces of short-term denudation in glacially impacted landscapes, an example
739 from the Western Alps: Journal of Geophysical Research – Earth Surface.
740 Gutenberg, B, and Richter, C.F., 1954, Seismicity of the Earth and Associated Phenomena:
741 Princeton University Press, Princeton, New Jersey, 245 pp.
742 Holt, W.E., Shen-Tu, B., Haines, J. and Jackson, J., 2000, On the determination of self-
743 consistent strain rate fields within zones of distributed continental deformation, In:
744 The History and Dynamics of Global Plate Motions: AGU Geophysical Monograph
745 Series, v. 121, 113–141.
746 Hoorn, C., Guerrero J., Sarmiento G.A., and Lorente, M.A., 1995, Andean tectonics as a
747 cause for changing drainage patterns in Miocene northern South America: Geology, v.
748 23, p. 237–240.
749 Jarvis, A., Reuter, H.I. , Nelson, A., and Guevara, E., 2008, Hole-filled SRTM for the globe
750 Version 4, available from the CGIAR-CSI SRTM 90m Database
751 (http://srtm.csi.cgiar.org).
752 Kirchner, J. W., Finkel, R. C., Riebe, C. S., Granger, D. E., Clayton, J. L., King, J. G., and
753 Megahan, W.F., 2001, Mountain erosion over 10 yr, 10 k.y., and 10 m.y. time scales:
754 Geology, v. 29, p. 591–594.
755 Kohn, B.P., Shagam, R., Banks, P.O., and Burkley, L.A., 1984, Mesozoic-Pleistocene fission
756 track ages on rocks of the Venezuelan Andes and their tectonic implications:
757 Geological Society of America Memoir 162, p. 365–384.
758 Koons, P.O., 2009, On the implications of low spatial correlation of tectonic and climate
759 variables in the western European Alps: Geology, v. 37, p. 863–864.
760 Lamb, S. and Davis, P., 2003, Cenozoic climate change as a possible cause for the rise of the
761 Andes: Nature, v. 425, p. 792–797.
762 Lague, D., 2010, Reduction of long-term bedrock incision efficiency by short-term alluvial
763 cover intermittency: Journal of Geophysical Research, v. 115, F02011, doi:
764 10.1029/2008jf001210.
765 McPhillips, D. and Brandon, M.T., 2010, Using tracer thermochronology to measure modern
766 relief change in the Sierra Nevada, California. Earth and Planetary Science Letters, v.
767 296, p. 373–383, doi: 10.1016/j.epsl.2010.05.022.

768 Mitchell, S.G. and Montgomery, D.R., 2006, Influence of a glacial buzzsaw on the height and
769 morphology of the Cascade Range in central Washington State, USA: Quaternary
770 Research, v. 65, p. 96–107.
771 Molnar, P. and England, P., 1990, Late Cenozoic uplift of mountain ranges and global climate
772 change: chicken or egg?: Nature, v. 346, p. 29–34.
773 Montgomery, D.R., Balco, G., and Willett, S.D., 2001, Climate, tectonics, and the
774 morphology of the Andes: Geology, v. 29, p. 579–582.
775 Montgomery, D.R., Brandon, M.T., 2002, Topographic controls on erosion rates in
776 tectonically active mountain ranges: Earth and Planetary Science Letters, v. 201, p.
777 481–489.
778 Mora, A., Parra, M., Strecker, M.R., Sobel, E.R., Hooghiemstra, H., Torres, V., and
779 Jaramillo, J.V., 2008, Climatic forcing of asymmetric orogenic evolution in the
780 Eastern Cordillera of Colombia: Geological Society of America Bulletin, v.120, p.
781 930–949.
782 Mora, A., Gaona, T., Kley, J., Montoya, D., Parra, M., Quiroz, L.I., Reyes, G., and Strecker,
783 M.R., 2009, The role of inherited extensional fault segmentation and linkage in
784 contractional orogenesis: a reconstruction of Lower Cretaceous inverted rift basins in
785 the Eastern Cordillera of Colombia: Basin Research, v. 21, p. 111-137.
786 Naranjo, M.E., and Duque, R., 2004, Estimación de la oferta de agua superficial y conflictos
787 de uso en la cuenca alta del Río Chama, Mérida, Venezuela: INCI, v. 29, p. 130–137.
788 Niu, F., Bravo, T., Pavlis, G., Vernon, F., Rendon, H., Bezada, M., and Levander, A., 2007,
789 Receiver function study of the crustal structure of the southeastern Caribbean plate
790 boundary and Venezuela: Journal of Geophysical Research, v. 112, B11308, doi:
791 10.1029/2006JB004802.
792 Parra, M., Mora, A., Sobel, E.R., Strecker, M.R., and Gonzalez, R., 2009, Episodic orogenic
793 front migration in the northern Andes: Constraints from low-temperature
794 thermochronology in the Eastern Cordillera, Colombia: Tectonics, v. 28, doi:
795 10.1029/2008TC002423.
796 Pindell, J.L., and Kennan, L., 2001, Kinematic evolution of the Gulf of Mexico and
797 Caribbean, in Fillon, R.H., Rosen, N.C., and Weimer, P., eds., Petroleum Systems of
798 Deep-Water Basins: Global and Gulf of Mexico Experience: GCSSEPM Foundation,
799 21st Annual Research Conference, Transactions: Houston, TX, Gulf Coast Section,
800 Society for Sedimentary Geology, p. 193–220.

801 Rahl, J.M., Ehlers, T.A. and van der Pluijm, B.A., 2007, Quantifying transient erosion of
802 orogens with detrital thermochronology from syntectonic basin deposits: Earth and
803 Planetary Science Letters, v. 256, p. 147–161.
804 Reiners, P. W., and Brandon, M.T., 2006, Using thermochronology to understand orogenic
805 erosion: Annual Reviews Earth Planetary Sciences, v. 34, p. 419–466.
806 Reiners, P. W., Ehlers, T. A., Mitchell, S.G., and Montgomery, D.R., 2003, Coupled spatial
807 variations in precipitation and long-term erosion rates across the Washington
808 Cascades: Nature, v. 426, p. 645–647.
809 Riebe, C. S., Kirchner, J. W., Granger, D. E., and Finkel, R. C., 2001a, Minimal climatic
810 control on erosion rates in the Sierra Nevada, California: Geology, v. 29, p. 447–450.
811 Riebe, C. S., Kirchner, J. W., Granger, D. E., and Finkel, R. C., 2001b, Strong tectonic and
812 weak climatic control of long-term chemical weathering rates: Geology, v. 29, p. 511–
813 514.
814 Ruhl, K.W., and Hodges, K.V., 2005, The use of detrital mineral cooling ages to evaluate
815 steady state assumptions in active orogens: An example from the central Nepalese
816 Himalaya: Tectonics, v. 24, TC4015, doi:10.1029/2004TC001712.
817 Schneider J. F., Pennington W. D., and Meyer R. P., 1987, Microseismicity and focal
818 mechanisms of the intermediate depth Bucaramanga Nest, Colombia: Journal of
819 Geophysical Research, v. 92, p.13913–13926.
820 Schubert, C., 1984, The Pleistocene and recent extent of the glaciers of the Sierra Nevada de
821 Merida, Venezuela: Erdwissenschaftliche Forschung , v. 18, p. 269–278.
822 Spotila, J.A., House, M.A., Niemi, N.A., Brady, R.C., Oskin, M. and Buscher, J.T., 2007,
823 Patterns of bedrock uplift along the San Andreas fault and implications for
824 mechanisms of transpresion: In A.B. Till, S.M. Roeske, J.C. Sample and D.A. Foster
825 (Eds.), Exhumation Associated with Continental Strike-Slip Fault Systems: Geological
826 Society of America Special Paper, v. 434, p. 15–33.
827 Stansell, N.D., Polyssar, P.J., and Abbott, M.B., 2006, Last glacial maximum equilibrium-line
828 altitude and paleo-temperature reconstructions for the Cordillera de Mérida,
829 Venezuelan Andes: Quaternary Research, v. 67, p. 115–127.
830 Stewart, R.J. and Brandon, M.T., 2004, Detrital-zircon fission-track ages for the "Hoh
831 Formation": Implications for late Cenozoic evolution of the Cascadia subduction
832 wedge: Geological Society of America Bulletin, v.116, p. 60–75.

833 Stock, G.M., Ehlers, T.A. and Farley, K.A., 2006, Where does sediment come from?
834 Quantifying catchment erosion with detrital apatite (U-Th)/He thermochronometry:
835 Geology, v. 34, p. 725–728.
836 Strecker, M.R. Alonso, R.N., Bookhagen, B., Carrapa, B., Hilley, G.E., Sobel, E.R., and
837 Trauth, M.H., 2007, Tectonics and climate of the southern central Andes. Annual
838 Review of Earth and Planetary Sciences, v. 35, p. 747–787.
839 Strecker, M.R., Alonso, R., Bookhagen, B., Carrapa, B., Coutand, I., Hain, M.P., Hilley, G.E.,
840 Mortimer, E., Schoenbohm, L., and Sobel, E.R., 2009,. Does the topographic
841 distribution of the central Andean Puna Plateau result from climatic or geodynamic
842 processes?: Geology, v. 37, p. 643–646.
843 Thomson, S.N., Brandon, M.T., Tomkin, J.H., Reiners, P.W., Vasquez, C. and Wilson, N.J.,
844 2010, Glaciation as a destructive and constructive control on mountain building:
845 Nature, v. 467, p. 313–317, doi: 10.1038/nature09365
846 Tranel, L.M., Spotila, J.A., Kowalewski, M.J. and Waller, C.M., 2011, Spatial variation of
847 erosion in a small, glaciated basin in the Teton Range, Wyoming, based on detrital
848 apatite (U-Th)/He thermochronology: Basin Research, v. 23, p. 571–
849 590,10.1111/j.1365-2117.2011.00502.x.
850 Tucker, G.E., and Whipple, K.X., 2002, Topographic outcomes predicted by stream erosion
851 models: Sensitivity analysis and intermodel comparison: Journal of Geophysical
852 Research, v. 107, B9, 2179, doi:10.1029/2001JB000162.
853 van der Hilst, R., and Mann, P., 1994, Tectonic implications of tomographic images of
854 subducted lithosphere beneath northwestern South America: Geology, v. 22, p. 451-
855 454.
856 Vermeesch, P., 2007, Quantitative geomorphology of the White Mountains (California) using
857 detrital apatite fission track thermochronology: Journal of Geophysical Research, v.
858 112, F03004, doi: 10.1029/2006JF000671.
859 Vernon, A.J., van der Beek, P.A., and Sinclair, H., 2009, Spatial correlation between long-
860 term exhumation rates and present-day forcing parameters in the western European
861 Alps: Geology, v. 37, p. 859–862.
862 Whipp, D.M. Jr., Ehlers, T.A., Braun, J., and Spath, C.D., 2009, Effect of exhumation
863 kinematics and topographic evolution on detrital thermochronometer data: Journal of
864 Geophysical Research, v. 114, F04014, doi:10.1029/2008JF001195.
865 Whipple, K.X., 2004, Bedrock rivers and the geomorphology of active orogens: Annual
866 Review of Earth and Planetary Sciences, v.32, p. 151–185.

867 Whipple, K.X., 2009, The influence of climate on the tectonic evolution of mountain belts:
868 Nature Geoscience, v. 2, p. 97–104.
869 Williamson, J.H., 1968, Least-squares fitting of a straight line: Canadian Journal of Physics,
870 v. 46, p.1845–1847.
871 Wilson, J.P., Gallant, J.C., 2000, Terrain Analysis: Principles and Applications: John Wiley &
872 Sons, Inc, 479 p.
873 Wittmann, H., von Blanckenburg, F., Kruesmann, T., Norton, K.P. and Kubik, P.W., 2007,
874 The relation between rock uplift and denudation from cosmogenic nuclides in river
875 sediment in the Central Alps of Switzerland: Journal of Geophysical Research, v. 112,
876 F04010, doi:10.1029/2006JF000729.
877 Wobus, C.W., Whipple, K.X., Kirby, E., Snyder, N.P., Johnson, J., Spyropolou, K., Crosby,
878 B. and Sheehan, D., 2006, Tectonics from topography: procedures, promise and
879 pitfalls: In S. Willett, N. Hovius, M. Brandon and D. Fisher (Editors), Tectonics,
880 Climate and Landscape Evolution: Geological Society of America Special Paper, v.
881 398, p. 55–74.
882

883 **Figure captions**

884

885 Fig. 1. A) Shaded digital elevation model (1-km resolution; Jarvis et al., 2008) showing
886 tectonic framework of northwestern South America. Col = Colombia; Ec = Ecuador; NAB =
887 Northern Andean Block; VA = Venezuelan Andes; BFS = Boconó fault; MB = Maracaibo
888 Block (Modified from Cediel et al., 2003). B) Geologic, structural and drainage map of the
889 Venezuelan Andes, modified from Case et al. (1990), Audemard et al. (2000) and Bermúdez
890 et al. (2010). Major fault systems are indicated (IFS: Icotea; BFS: Boconó; CSAFS: Central-
891 Sur Andino; CFS: Caparo; VFS: Valera and BurF: Burbusay). Inset shows major tectonic
892 blocks of the Venezuelan Andes (CATB: Cerro Azul Thrust; CB: Caparo; EB: Escalante;
893 ECB: El Carmen; SLCB: Sierra La Culata; SNB: Sierra Nevada, and TB: Trujillo). C)
894 Simplified structural cross section of central Venezuelan Andes. SLC: Sierra La Culata, SN:
895 Sierra Nevada de Mérida (Modified from Colletta et al., 1997).

Fig. 2. Shaded 90-m resolution digital elevation model of the Venezuelan Andes (Jarvis et al., 2008) with location of bedrock apatite fission-track ages (white circles) and detrital samples (star symbols). Thick dark gray polygons indicate catchment boundaries. Histograms show distribution of detrital AFT ages for the different samples (note logarithmic age scale); the grain-age distributions were decomposed into peak age components using binomial peak fitting (Stewart and Brandon, 2004). Peak ages (P1, P2, P3) are indicated, with the number of grains (percentage in parentheses) that composes each population.

Fig. 3. Comparison of measured (continuous black line; dashed lines indicate 95% confidence limits) and predicted bedrock (grey lines indicate 1000 random samples) cumulative density age functions (CDF) for the Chama catchment; inset shows probability-density functions (PDF) for comparison. (A) shows a comparison for random (un-weighted) sampling of bedrock age distribution; (B) shows results for a weighted age distribution where the probability of sampling a particular bedrock age is a function of the associated long-term exhumation rate relative to the average exhumation rate (see text for discussion). Numbers show average Kolmogorov Smirnov (KS) and Kuiper (KT) statistics, with associated p-values, which test the null hypothesis (H_0: the distributions are indistinguishable). The number of simulations that fail the KS and KT test at a significance level $p = 0.05$ is also indicated.

Fig. 4. (A) 5-km radius relief across the Venezuelan Andes, draped over a shaded relief image. Peaks over 4300 m elevation in the central part of the range are indicated by triangles. Mean relief for each analyzed catchment is summarized in Table 2. (B) Average precipitation pattern (m yr^{-1}) across the Venezuelan Andes, compiled from various databases (see text for details), overlain on shaded relief image of topography

921

922 Fig. 5. (A) Major active faults systems (modified from Audemard et al., 2000) and seismicity
923 database compiled for the period 1911-2011 from digital libraries at Universidad de Los
924 Andes (http://lgula.ciens.ula.ve/) and FUNVISIS (http://www.funvisis.org.ve). (B) Cumulated
925 seismic energy released, calculated from the earthquake database. Individual earthquakes with
926 $M > 5$ occurring outside the Venezuelan Andes are indicated (1: 1993/12/31, 70.70 W / 9.65
927 N, $M_w = 5.4$; 2: 2001/12/21, 70.96 W / 8.17 N, $M_w = 5.6$; 3: 2006/01/03, 71.92 W /9.89 N, M_w
928 = 5.0; 4: 2006/08/04, 70.65 W / 9.97 N, $M_w = 5.2$; 5: 1995/12/29, 70.26 W / 9.75 N, $M_w = 5.3$;
929 6: 1998/02/12, -70.23 W / 9.14 N, $M_w =$ 5.6). (C) Seismic strain rate as predicted from the
930 distribution and magnitude of earthquakes and the maximum earthquake magnitude M_{max}, of
931 each catchment using a 0.5° × 0.5° binning of the data (see text for explanation).
932

933 Fig. 6. Average logarithmic stream power index maps across the Venezuelan Andes. Left
934 columns (A, C and E) take spatially variable precipitation into account (stream power
935 calculated following equation 7); right columns (B, D, F) assume spatially constant
936 precipitation (stream power calculated following equation 6): A, B) Total Stream Power
937 (TSP; $m = n = 1$ in equations 6, 7); C, D) Unit Stream Power (USP; $m = 0.5$; $n = 1$); E, F)
938 Shear Stress (SSP; $m = 0.33$; $n = 0.67$).
939

940 Fig. 7. Correlation plots for: A) 5-km relief, B) present-day precipitation, C) seismic energy
941 release, D) seismic strain rate, E) Total stream power (uniform precipitation) and F) Total
942 stream power (spatially variable precipitation), all versus exhumation rate. Released seismic
943 energy was calculated from the map of cumulated seismic energy release within 25-km radius
944 windows around each earthquake (Figure 3B). Seismic strain rate was calculated only for
945 catchments with more than 10 earthquakes following equation (4) in the text. For all
946 correlations, r is the correlation coefficient calculated for a least-square regression line

947 without considering errors bars, and r_w is the correlation coefficient calculated for the
948 Williamson (1968) regression line.
949
950
951
952 **Supplementary Material**
953
954 Figure S1. Cumulative density plots of single-grain ages for the seven catchments analyzed in
955 this study.
956
957 Table S1. Results of Kolmogorov-Smirnov equality test for the cumulative density
958 distributions of single-grain ages of different catchments shown in Figure S1. For each couple
959 of catchments, the KS-statistic and the corresponding *p*-value testing the null-hypothesis that
960 the sample distributions are different are given. In blue, comparisons that pass the KS-test (i.e.
961 have similar age distributions), in bold red font, comparisons that fail the KS-test.

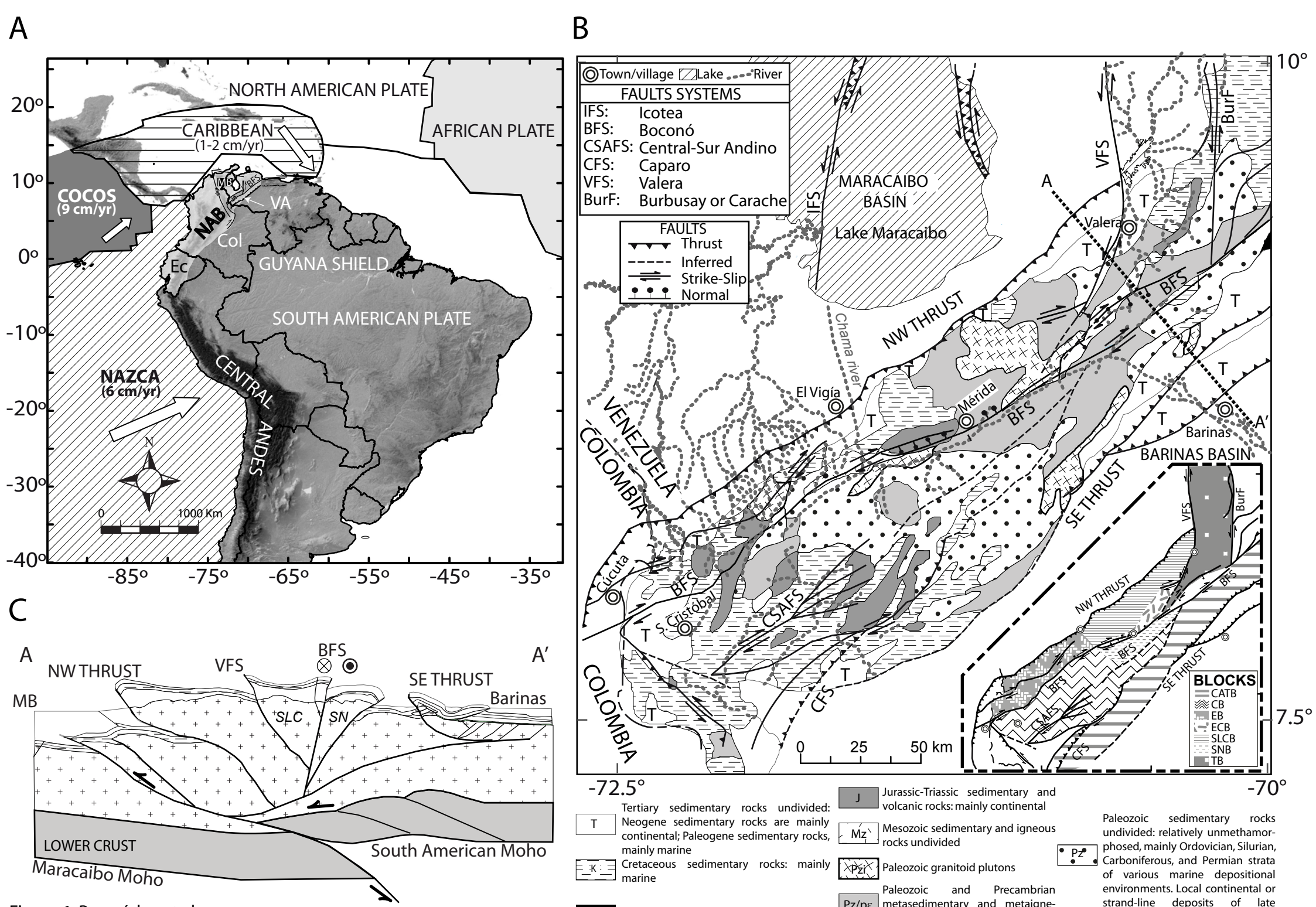

Figure 1. Bermúdez et al.

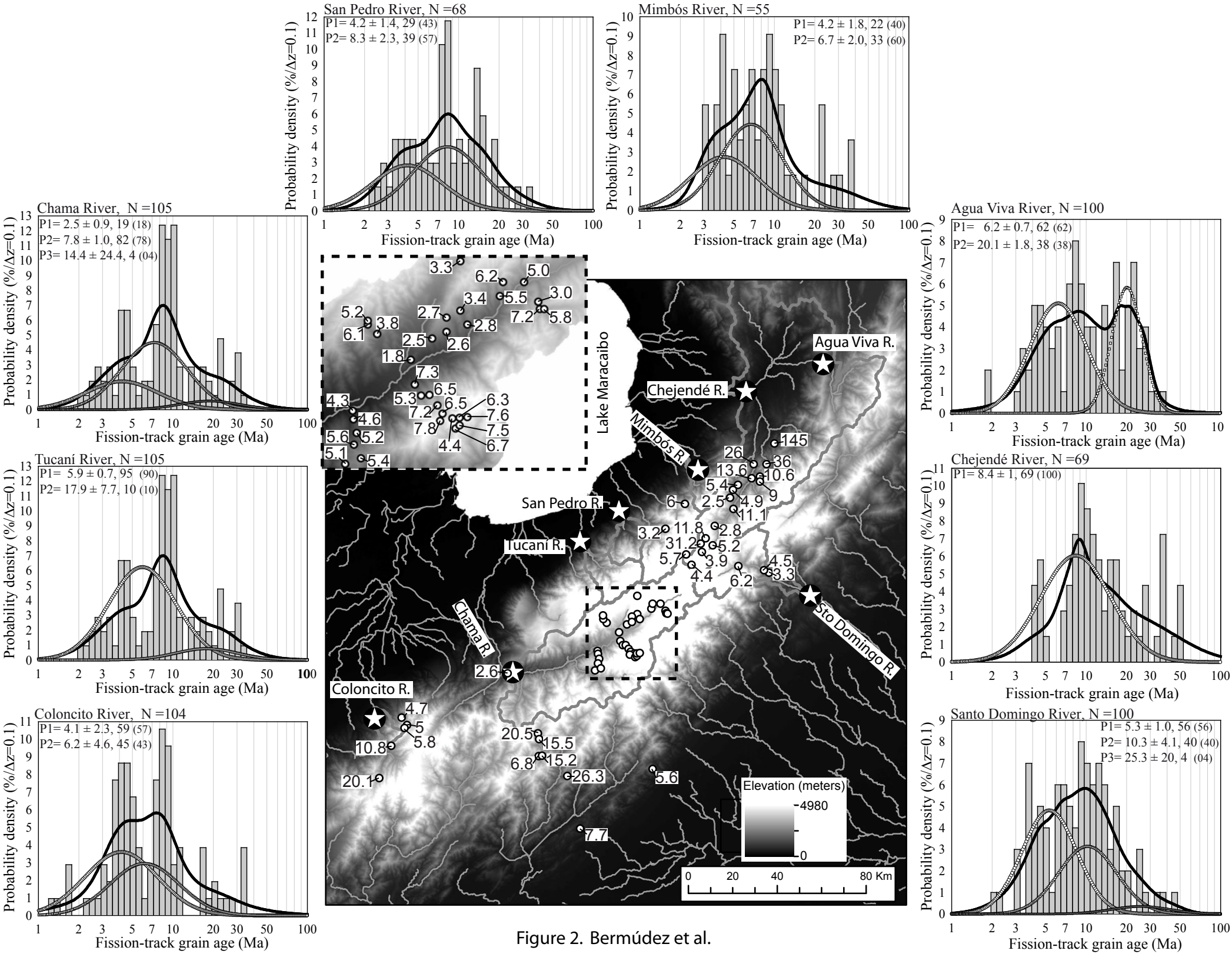

Figure 2. Bermúdez et al.

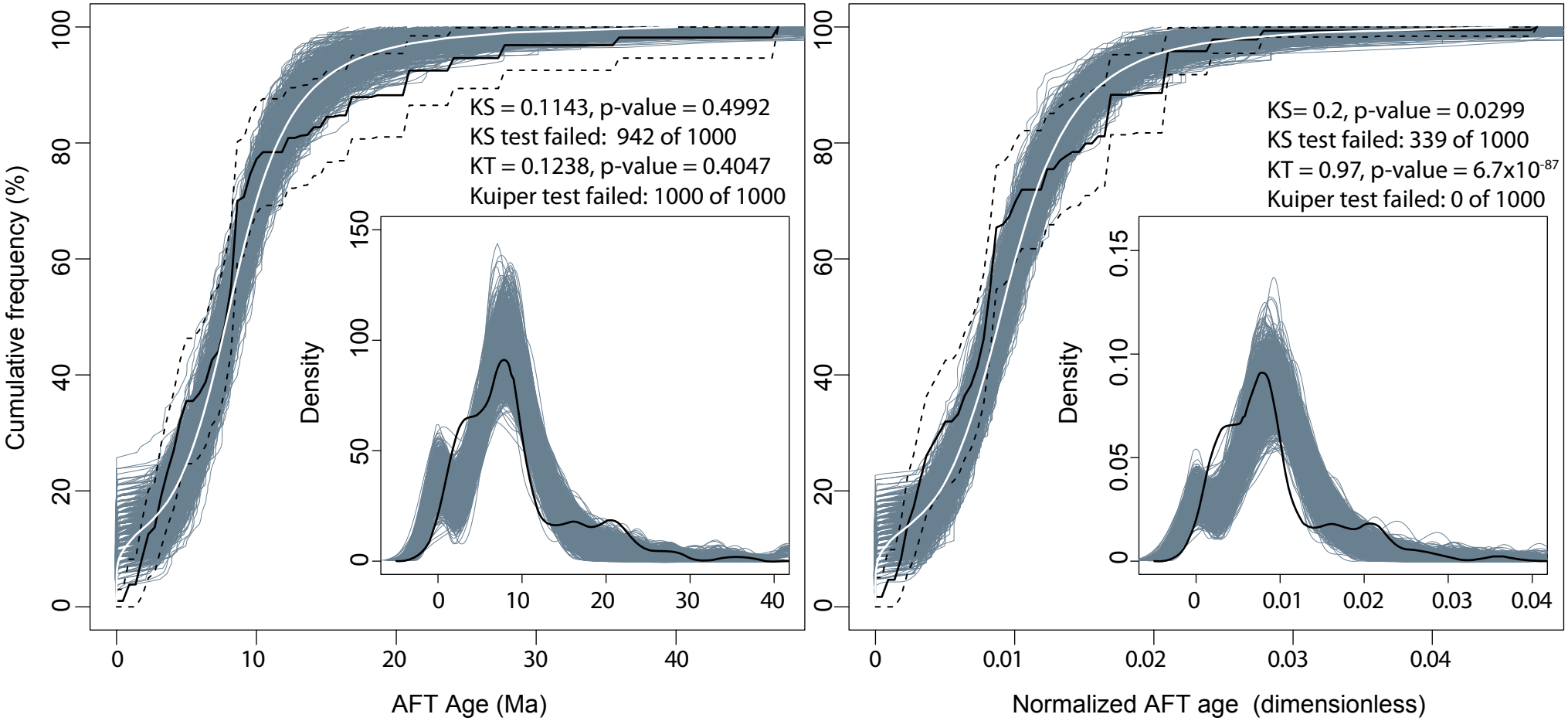

Figure 3. Bermúdez et al.

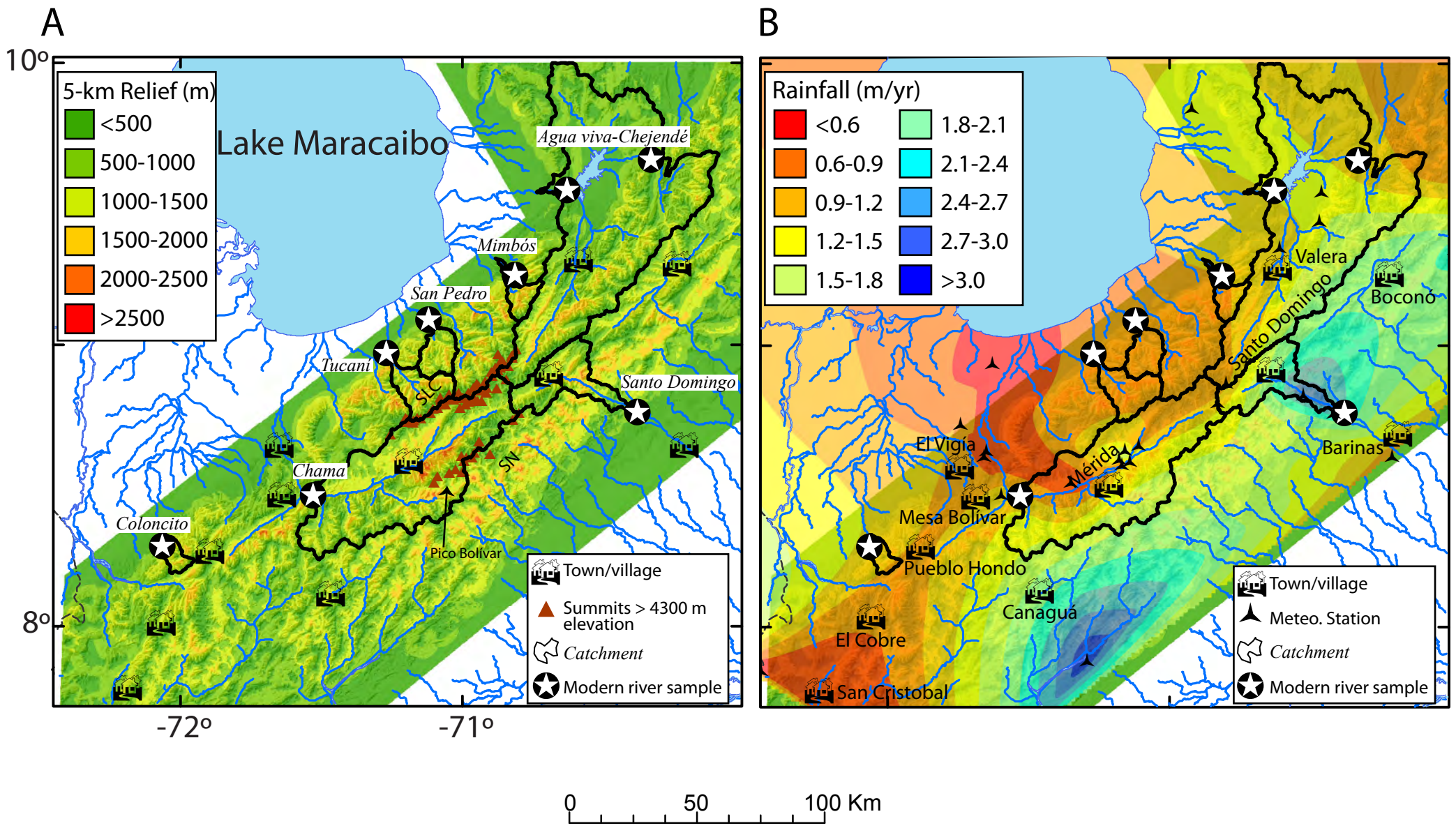

Figure 4. Bermúdez et al.

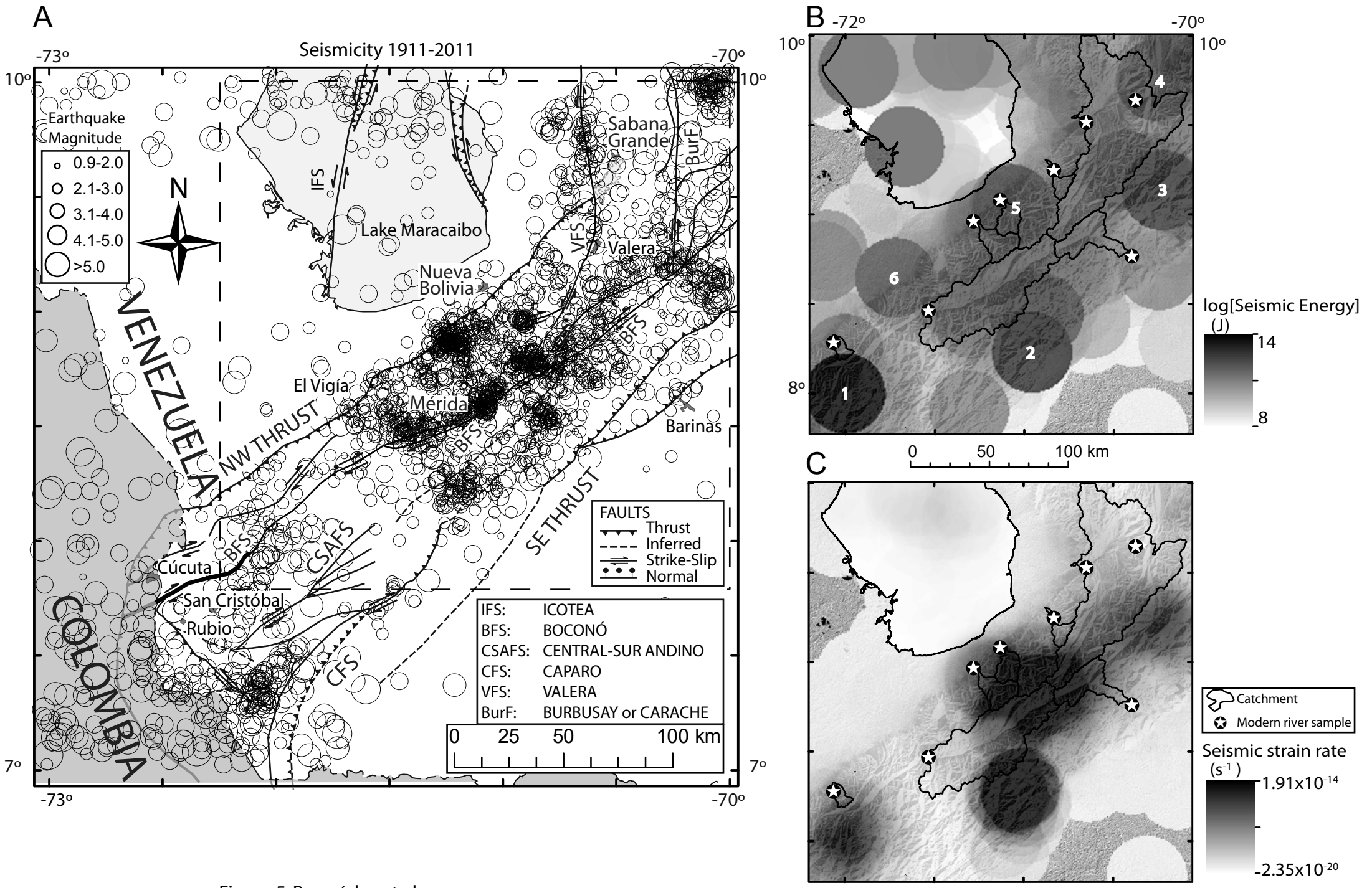

Figure 5. Bermúdez et al.

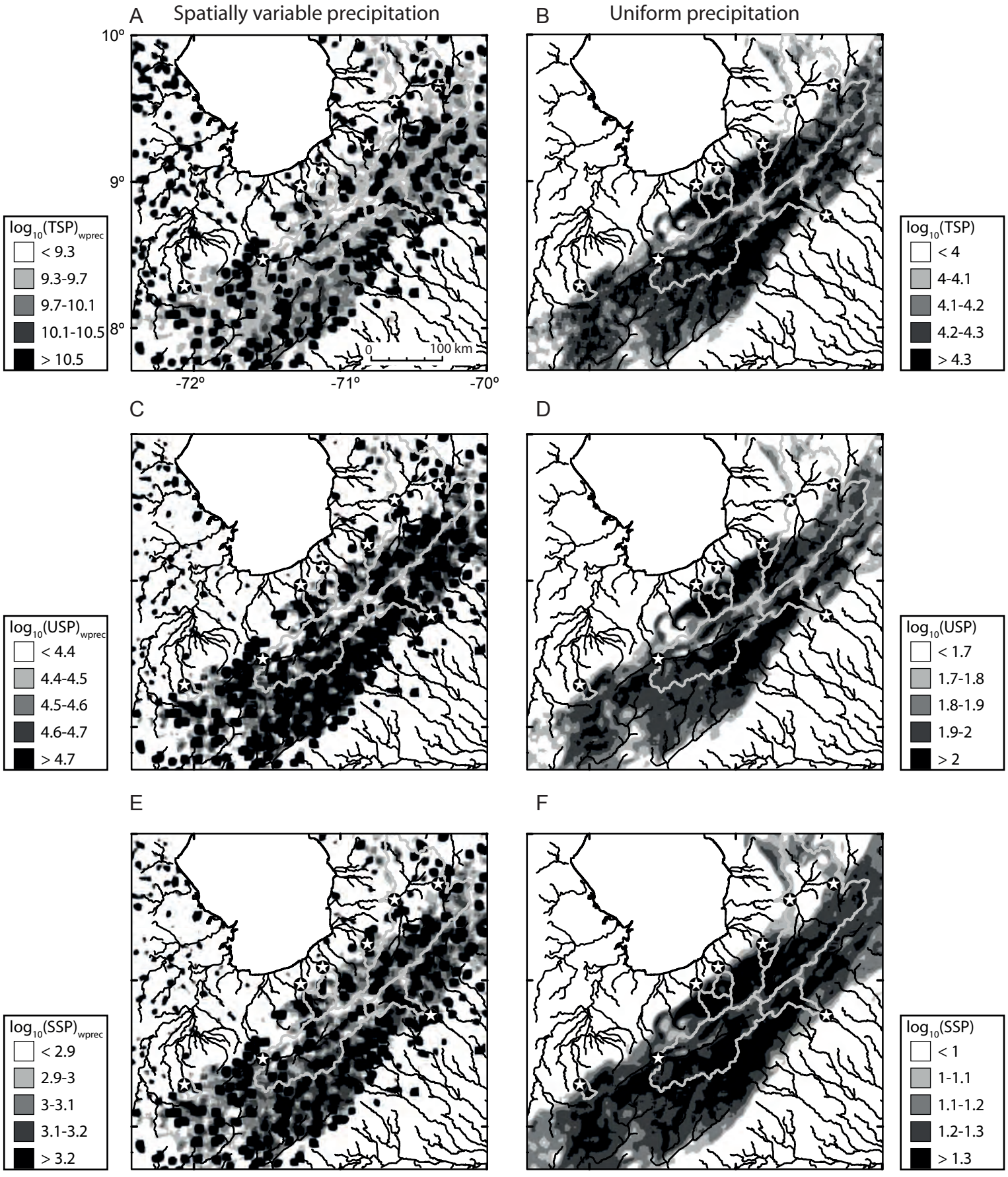

Figure 6. Bermúdez et al.

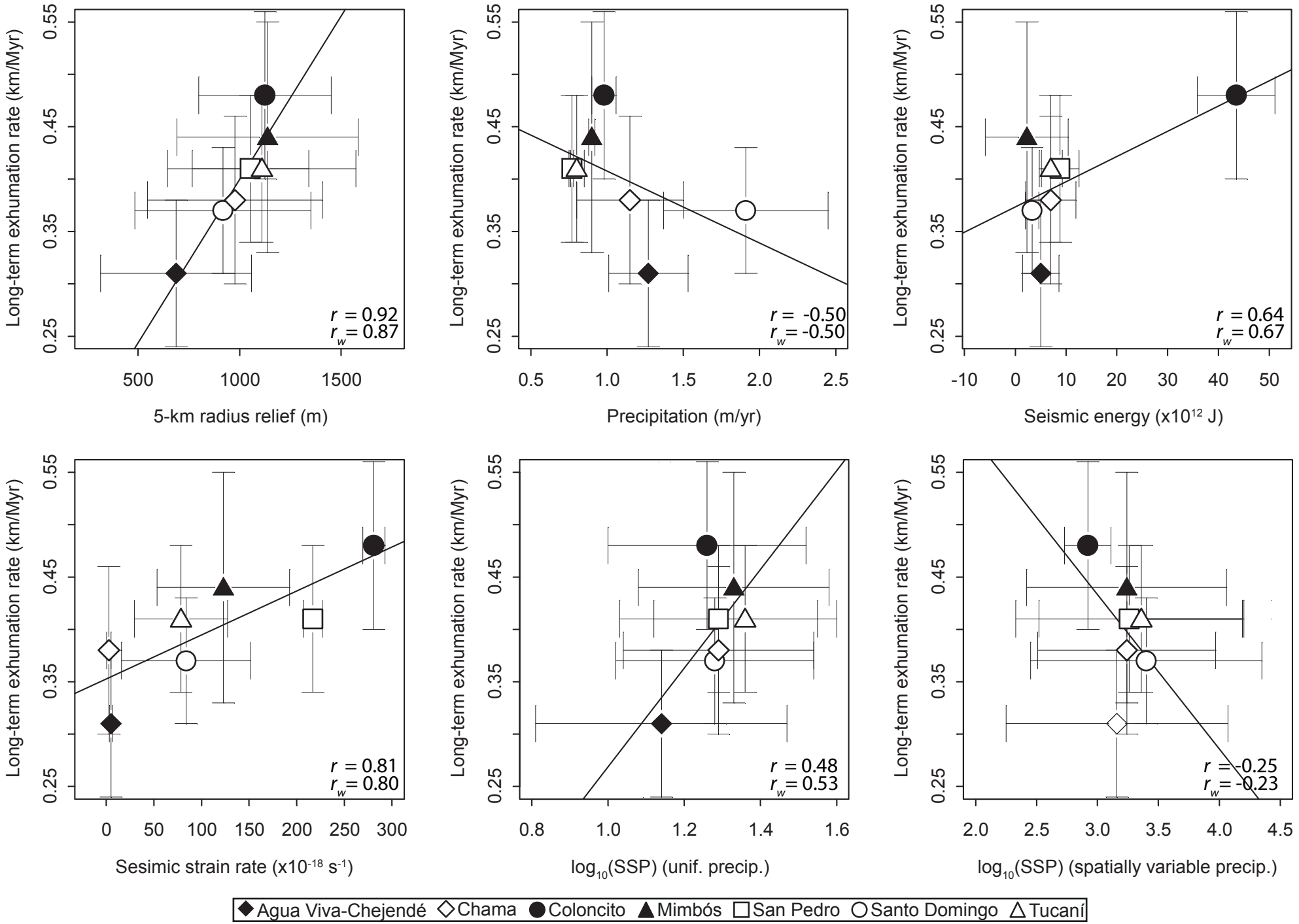

Fig. 7. Bermúdez et al.

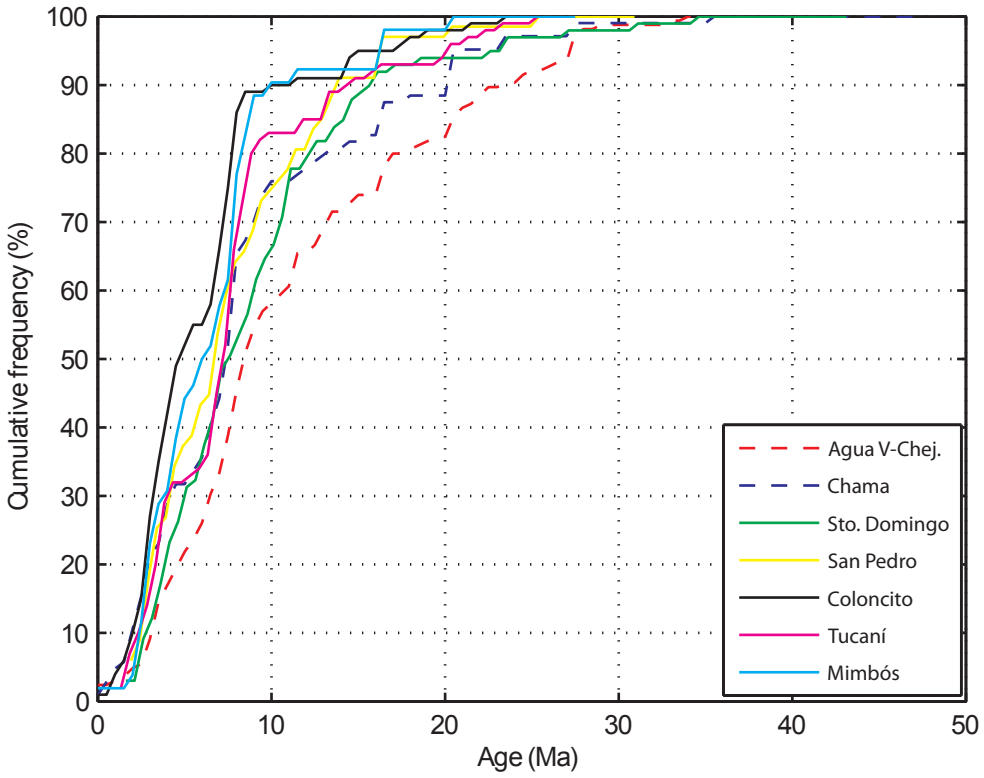
Qumulative frequency (%)
Age (Ma)
0
10
20
30
40
50
60
70
80
90
100
Agua V-Chej.
Chama
Sto. Domingo
San Pedro
Coloncito
Tucaní
Mimbós